Earth and Planetary Science Letters 412 (2015) 209–219

Contents lists available at ScienceDirect

Earth and Planetary Science Letters

www.elsevier.com/locate/epsl

The effect of pressurized magma chamber growth on melt migration and pre-caldera vent locations through time at Mount Mazama, Crater Lake, Oregon

Leif Karlstrom [a,*], Heather M. Wright [b], Charles R. Bacon [c]

[a] Department of Geological Sciences, University of Oregon, 1272 University of Oregon, Eugene, OR 97403, USA
[b] U.S. Geological Survey, Cascades Volcano Observatory, 1300 SE Cardinal Court, Building 10, Suite 100, Vancouver, WA 98683, USA
[c] U.S. Geological Survey, 345 Middlefield Road, Menlo Park, CA 94025, USA

ARTICLE INFO

Article history:
Received 6 January 2014
Received in revised form 25 October 2014
Accepted 1 December 2014
Available online xxxx
Editor: T. Elliott

Keywords:
Mount Mazama
magma chambers
eruptive history
Crater Lake

ABSTRACT

The pattern of eruptions at long-lived volcanic centers provides a window into the co-evolution of crustal magma transport, tectonic stresses, and unsteady magma generation at depth. Mount Mazama in the Oregon Cascades has seen variable activity over the last 400 ky, including the 50 km^3 climactic eruption at ca. 7.7 ka that produced Crater Lake caldera. The physical mechanisms responsible for the assembly of silicic magma reservoirs that are the precursors to caldera-forming eruptions are poorly understood. Here we argue that the spatial and temporal distribution of geographically clustered volcanic vents near Mazama reflects the development of a centralized magma chamber that fed the climactic eruption. Time-averaged eruption rates at Mount Mazama imply an order of magnitude increase in deep magma influx prior to the caldera-forming event, suggesting that unsteady mantle melting triggered a chamber growth episode that culminated in caldera formation. We model magma chamber–dike interactions over ~50 ky preceding the climactic eruption to fit the observed distribution of surface eruptive vents in space and time, as well as petrologically estimated deep influx rates. Best fitting models predict an expanding zone of dike capture caused by a growing, oblate spheroidal magma chamber with 10–30 MPa of overpressure. This growing zone of chamber influence causes closest approaching regional mafic vent locations as well as more compositionally evolved Mazama eruptions to migrate away from the climactic eruptive center, returning as observed to the center after the chamber drains during the caldera-forming eruption.

1. Introduction

Long-lived volcanic centers commonly exhibit a wide variety of eruptions, including those that emanate from a centralized volcanic edifice as well as from regionally scattered monogenetic vents and shield volcanoes. The pattern of eruptions is generally highly variable in space and episodic in time: even from a single volcanic edifice, eruption style may vary widely in magnitude and intensity. Physical controls on the spatial and temporal organization of eruptions are poorly constrained. At some volcanic centers, a long history of repeated activity includes explosive eruptions of sufficient size to cause collapse of the central edifice, producing a caldera. Evaluation of which volcanoes are capable of caldera-forming eruptions (thereby defining the maximum potential hazard at a given center; Marzocchi and Bebbington, 2012) requires finding evidence for the presence of a large volume of eruptible magma at depth. Such evidence may be found in long-term patterns of eruptive activity that precede caldera collapse, outputs of the subsurface crustal magma transport network.

Volcanically active regions also exhibit spatially variable eruption patterns, such as the common along-strike volcanic vent density variation observed in active volcanic arcs (Siebert et al., 2011). This spatial localization is inexorably tied to temporal variability in eruption style and composition. A variety of mechanisms have been proposed for focusing of melt towards volcanic centers, all of which fall into three general classes of models for volcano spacing: "bottom up" models propose localization in the melt source region through buoyancy instabilities (e.g., Marsh and Carmichael, 1974; Olson and Singer, 1985), "top down" models propose dike focusing through stress interactions with surface edifice loads (e.g., Muller et al., 2001), while "internal" models rely on stress interactions between magma chambers – storage zones in which melt fractions are high enough that pressure gradients are homogenized by flow – and dikes to generate spatially discrete volcanic centers (e.g., Karlstrom et al., 2009).

* Corresponding author.
E-mail address: leif@uoregon.edu (L. Karlstrom).

http://dx.doi.org/10.1016/j.epsl.2014.12.001
0012-821X/

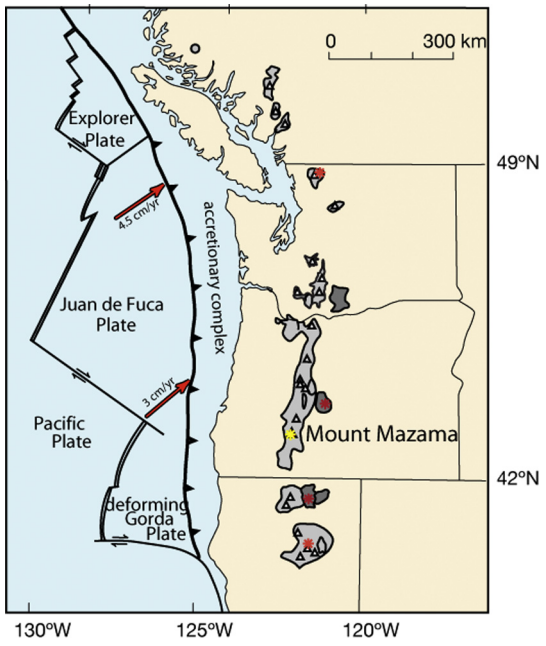

Fig. 1. Location of Mount Mazama and Crater Lake caldera in the Cascades chain (yellow asterisk). Other identified Quaternary calderas are shown with red asterisks. Modified after Hildreth (2007). (For interpretation of the references to color in this figure legend, the reader is referred to the web version of this article.)

Here we use the eruptive history at Mount Mazama, Oregon (Fig. 1; Bacon and Lanphere, 2006; Wright et al., 2012), to probe evolving subsurface architecture of magma transport leading to the Mazama climactic caldera-forming eruption at ca. 7.7 ka (CFE hereafter) through application of a mechanical model for the plumbing system. Trends in erupted compositions and volumes, along with the caldera structure itself, indicate that an evolving magma chamber played a key role in the style and distribution of surface volcanism. Therefore we focus efforts on the "internal" class of models described above, using known locations and timing of eruptive episodes over 55 ky along with petrologically based estimates of melt influx to constrain models for silicic chamber growth and dike capture. Although the idea that mafic magma may be trapped or stalled by a shallow, less dense magma reservoir is not new (e.g., Walker, 1974; Smith and Shaw, 1975; Hildreth, 1981; de Silva, 1989), here we hypothesize that overpressure within the growing climactic chamber generates a deviatoric stress field that reorients more distant rising dikes (Karlstrom et al., 2009, 2010) to control the rate of chamber growth and surface eruption locations.

2. Mount Mazama eruptive history

The geologic record of Mount Mazama includes remarkable exposures of volcanic sequences in the caldera walls at Crater Lake that offer a rare opportunity to see otherwise buried deposits. Volcanic activity at Mount Mazama has persisted for >400 ky, with andesite and low-silica dacite lava flows dominating the eruptive products from the central volcano (Bacon and Lanphere, 2006; Bacon, 2008). The appearance of silicic dacites and rhyodacites occurs late in the eruptive sequence (71 ka and 27 ka, respectively), culminating in the 50 km^3 zoned eruption of Mount Mazama (CFE) that led to caldera collapse ca. 7.7 ka (Bacon, 1983; cf. 7627 ± 150 cal. yr. BP age of Zdanowicz et al., 1999).

For the present study we have compiled a database of Mazama volcanism that includes compositions, ages, and volumes of eruptive units along with vent locations (additional discussion of mapping and data selection in the Supplementary Material). Fig. 2 shows the distribution of eruptive vent locations for the last 400 ky, as a function of map distance (in km) from the caldera center for the Mazama climactic eruption, along with corresponding volumes (symbol size) and *maximum* SiO_2 contents (symbol color). Eruptions with increasing maximum silica content through time (Bacon and Lanphere, 2006; their Fig. 7) and a weak correlation between erupted volume and maximum silica content for the entire dataset (correlation coefficient 0.229, p-value 0.029) imply increased crustal storage in time (e.g., Bacon and Druitt, 1988).

This work focuses on the last 55 ky of Mazama eruptive history leading up to CFE, in which vents appear progressively farther from the climactic caldera center (Fig. 2.B). Starting with near-summit domes of the dacite of Munson Valley and the mingled lava of Williams Crater (both ~35 ka), evolved silicic eruptions migrate steadily away from the climactic center, with some radial dike controlled patterns that reflect shallow fault control (Bacon, 2008), until two substantial rhyodacitic units (Llao Rock preclimactic rhyodacite and Cleetwood preclimactic rhyodacite) erupted near the climactic center decades before CFE. These eruptions are interpreted by Bacon (1983) as failed attempts or precursors to the climactic eruption. Nowhere prior in the Mazama history do regional eruptions and evolved silicic eruptions spatially migrate away from a large volume eruption (and CFE is the largest eruption recorded). Furthermore, silicic vents appear ~6 km farther away from the climactic center during this period than elsewhere in the eruptive history (Fig. 2.A). Closest approaching regional mafic eruptions occur farther from the center than the evolved Mazama eruptions. After the caldera-forming event, eruptive activity again appears close to the climactic vent location.

2.1. Mazama melt influx estimates

We model melt evolution at Mazama using the Rhyolite MELTS program (RMELTS; Gualda et al., 2012). The initial magma composition in these petrologic simulations is equivalent to the whole rock composition of basaltic andesite of Red Cone (unit abbreviations br and brp; Bacon, 2008), a monogenetic volcano northwest of Crater Lake taken as a proxy for primary compositions of magmas entering the Mazama plumbing system. Additional discussion of these samples and RMELTS models may be found in the Supplementary Material.

The range of erupted magma compositions at Mount Mazama reflects a combination of fractional crystallization, assimilation and recharge (Bacon and Druitt, 1988; Bacon et al., 1994; Bacon and Lanphere, 2006; Wright et al., 2012). However much of this compositional variation can be explained as due to crystallization from parental melt (Bacon and Druitt, 1988). Therefore, we do not include magma mixing, recharge, or assimilation in RMELTS models. We recognize that recharge likely has important effects on magma chamber compositions in long-lived reservoirs such as at Mazama (e.g., Eichelberger, 1974). Our goal is not to model the details of Mazama compositional evolution but rather general trends, for which a melt mass fraction-composition parameterization based on fractional crystallization is sufficient.

We assume isobaric crystallization at 3 kbar with initial $H_2O = 1$ wt%, fitting compositional data to find a polynomial relation between melt mass fraction and wt% SiO_2 (Supplementary Material Fig. S1)

$$\%\,\text{melt} = 48809.2 - 2973.58X_{SiO_2} + 67.932X_{SiO_2}^2 - 0.6888X_{SiO_2}^3 + 0.0026X_{SiO_2}^4, \quad (1)$$

where X_{SiO_2} is the weight percent SiO_2 in the melt.

Eruptive volumes and ages are then corrected via Eq. (1) to infer primary melt influx (Fig. 3) using a moving average over a

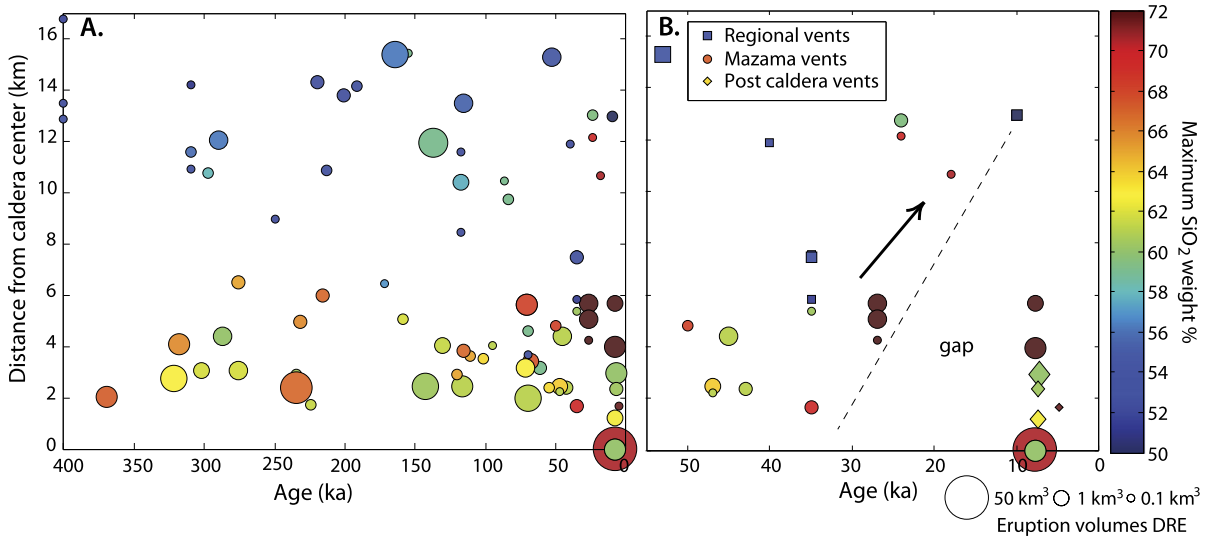

Fig. 2. A. Mazama region eruptive history since 400 ka, plotted against map distance from the center of Crater Lake caldera. Symbol size scales with eruption volume (Dense Rock Equivalent DRE) while symbol color is maximum silica content. **B.** Eruptive history since 55 ka separated into "Mazama" eruptions fed from the long-lived magma system and "regional" eruptions from High Cascades monogenetic and shield volcanoes, and post-caldera eruptions. Arrow indicates migration of regional and silicic Mazama vents away from the caldera center preceding the climactic eruption, creating a gap near the eventual caldera where no eruptions occur. (For interpretation of the references to color in this figure legend, the reader is referred to the web version of this article.)

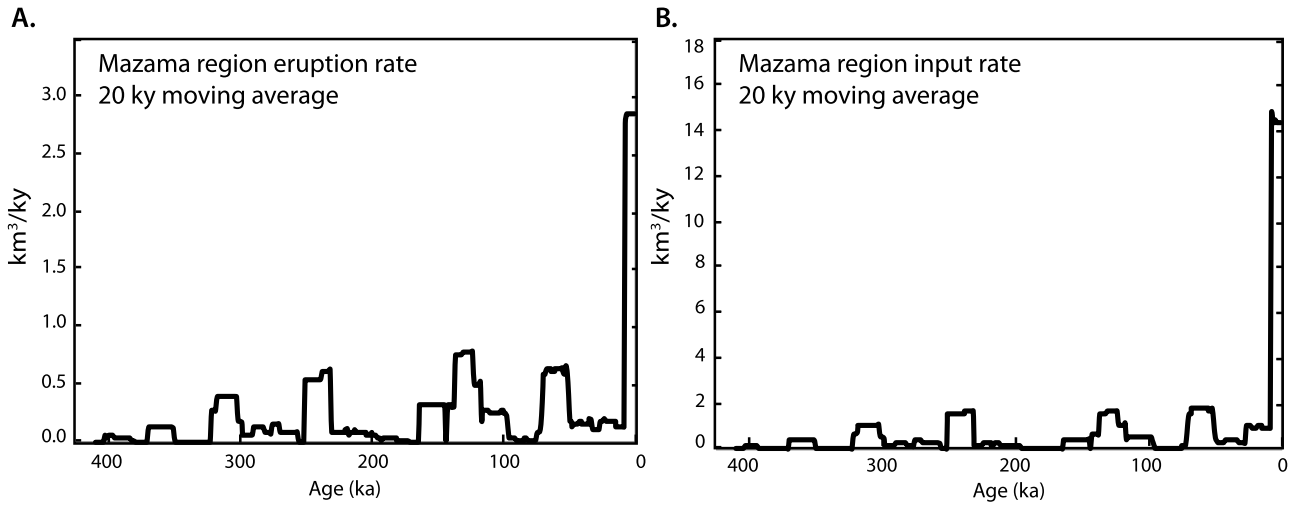

Fig. 3. A. 20 ky moving average of eruptive flux in the Mazama region. **B.** Eruptive flux corrected for fractional crystallization using Eq. (1), an estimate of primary magmatic input rate. The inferred influx increase in the last time bin is due to the CFE.

time window of 20 ky (where the window includes eruption information that precedes the age of interest). These influx estimates are a lower bound due to incomplete preservation of lavas, probable effect of recharge, and possible un-erupted residuum. Different choices of window for time averaging somewhat affect the overall magnitudes but do not affect the pattern of inferred input (Supplementary Material).

Stratovolcanoes, in general, grow in spurts (Hildreth, 2007). That an increase in magma input rate could trigger caldera-forming eruption of an evolved magma storage reservoir has long been suggested (e.g., Shaw, 1985), as has a general correlation between eruption volume and repose time (e.g., Smith, 1979). White et al. (2006) plots crystal residence times vs. eruptive repose intervals, arguing that large eruptions require multiple intrusions before eruption, though not necessarily that the rate increased. At Mazama, average eruption rates corrected for fractional crystallization over 400 ky suggest that magma influx increased by as much as an order of magnitude prior to the climactic eruption (Fig. 3.B).

2.2. Statistics of the vent distribution

Eruptive vents in the Mazama region are a proxy for subsurface magma transport processes. Statistical characterization of vent locations through time provides a predictive measure to compare proposed crustal transport pathways with the surface. The null hypothesis is a Poissonian spatial vent distribution, in which each eruption location is random and independent of others. This distribution is found at some monogenetic cone fields although many others deviate from it (e.g., Wadge and Cross, 1989; Connor and Hill, 1995). A Poissonian vent distribution would imply negligible control of subsurface magma storage zones on vent locations.

We apply a nearest neighbor analysis to the Mazama vicinity that uses statistics derived from a Poisson Nearest Neighbor test (Baloga et al., 2007)

$$R = \frac{\mu}{\mu_s}, \qquad C = \frac{\mu - \mu_s}{\phi_s} \tag{2}$$

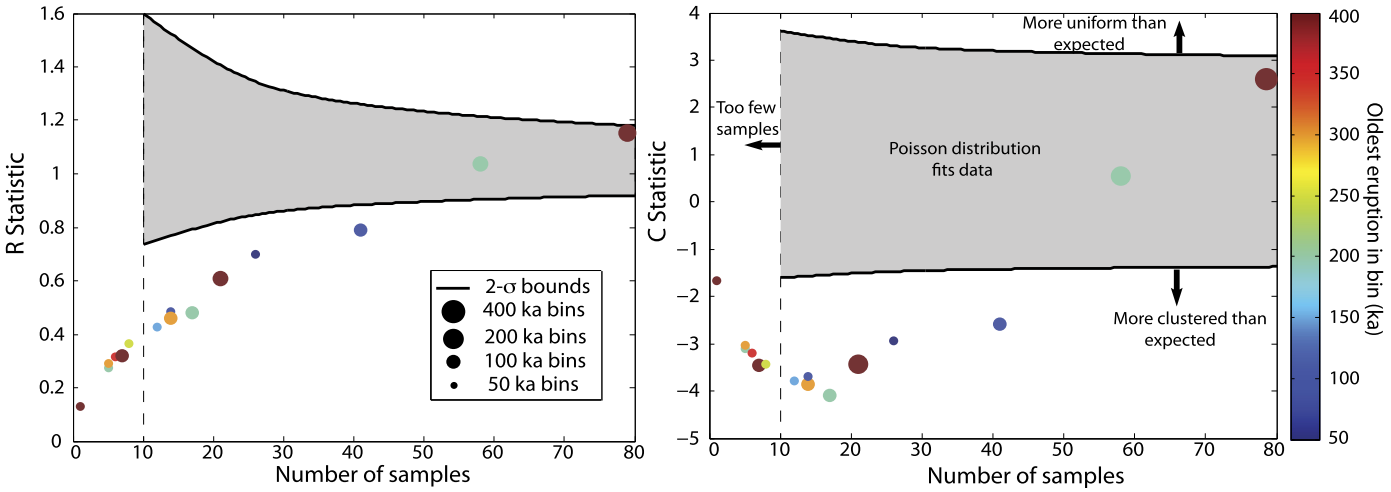

Fig. 4. Nearest neighbor analysis of eruptive vent locations, using the 400 ky eruptive history of the Mazama region from Fig. 2 divided into bins to test for Poissonian spatial vent distribution. Symbol color corresponds to oldest eruption in a bin, while symbol size corresponds to length in ky of bins. Points that lie below the gray sample size dependent 2σ bounds indicate a clustered distribution, which is the case for bin sizes less than 400 ky. (For interpretation of the references to color in this figure legend, the reader is referred to the web version of this article.)

Here μ is the mean nearest neighbor Euclidean distance observed in the dataset, while μ_s and ϕ_s are the mean and standard deviation of nearest neighbor distances drawn from a Poisson distribution. These test statistics provide a measure for the randomness of vent distributions: large R and C values indicate a tendency toward uniform spacing of vents, while small values indicate clustering. R and C within a sample-size dependent standard error distance of unity indicate a Poissonian vent distribution (Fig. 4).

Applied to the entire 400 ky eruptive history (largest symbols in Fig. 4), these statistics would imply that vents are distributed randomly, consistent with a Poisson distribution. However, this ignores temporal variations of eruptive output. If we decrease the temporal windows for computing the test statistics to 200 ky, eruptions exhibit more clustering behavior than is expected by a Poisson model. The distribution of surface eruptions at Mazama is thus consistent with some focusing mechanism at depth that guides vent locations over the entire eruptive history. Shifts in the center of eruptive focus are well documented at Mazama (Bacon and Lanphere, 2006), are common throughout Quaternary Cascades volcanism and otherwise (e.g., Marti and Gudmundsson, 2000; Hildreth, 2007), so it is not surprising that temporally resolved eruptive data are necessary to observe spatial clustering.

Statistical analysis applied to the time domain in our dataset (using time between eruptive episodes or inter-event times) does not yield similar results. Of course, temporal statistics are considerably less well constrained than in the spatial domain. Age errors are much larger than errors in vent location, mapped eruptive units may contain more than one eruption, and roughly a quarter of eruptive units in the last 200 ky have overlapping estimated ages. Nevertheless, for completeness we test for Poissonian behavior in inter-event times in the database. We normalize unique inter-event times by the average inter-event time, then follow the procedure of Marzocchi and Zaccarelli (2006).

Similar to our spatial study, the test statistic

$$\eta = \frac{\phi_t}{\mu_t} \tag{3}$$

where μ_t is the mean inter-event time and ϕ_t is the standard deviation of inter-event times, provides the metric to test for Poissonian behavior (Cox and Lewis, 1966). $\eta > 1$ indicates clustering while $\eta < 1$ is more periodic in time than the null hypothesis of a random distribution of inter-event times.

We determine the significance of this statistic by comparing η as calculated from data to 1000 synthetic Poissonian distributions ($\eta_s = 1$). The distributions η_s have the same number of eruptions or eruptive units as the dataset they are compared to. Significance α is then calculated as $\alpha = 2 \times \min(C^+, C^-)$, where C^+, C^- are the fraction of synthetic simulations for which $\eta_s \geq \eta$ and $\eta_s < \eta$, respectively (Marzocchi and Zaccarelli, 2006).

We perform this test on the entire set (eruptions <400 ky), and on smaller temporal subsets (<200 ky and <100 ky). In all cases we cannot reject the Poisson distribution at a >95% confidence level. We do not test for higher order Poisson-type distributions that may more accurately account for history dependence of eruption timing (Marzocchi and Zaccarelli, 2006; Nathenson et al., 2012). For the purposes here, eruption times are difficult to distinguish from a random distribution, while eruption locations are demonstrably clustered, implying interaction with and possibly control by a long lived centralized magma storage zone.

3. Model for an evolving Mazama plumbing system

A variety of observations thus suggest that magma storage times increased prior to the CFE, and that surface eruption locations reflect the influence of a focusing zone that defines the Mazama volcanic center. Eruptive episodes during the ~40–50 ky preceding caldera formation show a migration of vents (both regional monogenetic and Mazama related) away from the CFE center. We hypothesize that the spatial and temporal gap in eruptive vents before the CFE reflects growth and/or pressurization of a shallow silicic crustal reservoir beneath the central Mazama edifice. To test this hypothesis, we develop a model for magma chamber growth fed by melt rising through dikes from the magma source region.

3.1. Magma chamber mechanics

The mechanical stability of magma chambers and their surrounding stress fields depends on a number of factors both internal and external to the chamber. In general, relative overpressure and/or buoyancy of stored magma with respect to host rocks in excess of isotropic lithostatic stress drive all mechanical magma chamber dynamics. However, chamber geometry, background stresses, and host rock rheology all contribute to the translation of this stress source to magma chamber failure and interactions with magma rising from depth (e.g., Dufek et al., 2013).

Observations of active magma chambers are limited to relatively small volume systems over short timescales (e.g., Anderson and Segall, 2011; Poland et al., 2012), while exhumed chambers provide an integrated frozen window into long-term magma transport and storage but do not resolve eruption-scale processes (e.g., Zak and Paterson, 2005; Coleman et al., 2004). Insights into magma chamber dynamics thus rely heavily on modeling. In general such models must account for complex elastic stresses (e.g., Gudmundsson, 2006), thermomechanical effects and time dependent viscoelastic/plastic behavior of host rocks (e.g., de Silva and Gregg, 2014; Currenti and Williams, 2014), making simple characterization of magma chamber behavior difficult.

However, most of the parameters relevant to magma chamber mechanics such as overpressure, crustal mechanical layering, host rock rheology, and chamber geometry are poorly constrained. Because of this, it is sufficient to model a much simpler system to test the plausibility of our hypothesis. Thus we model the Mazama magma chamber as a uniformly overpressured oblate spheroidal cavity in an elastic half space.

We solve the equations of quasi-static linear elasticity in an isotropic solid

$$\frac{\partial \sigma_{ij}}{\partial x_j} = 0, \tag{4}$$

$$\sigma_{ij} = \lambda_E \epsilon_{kk} \delta_{ij} + 2\mu_E \epsilon_{ij}, \tag{5}$$

where σ is the stress tensor, ϵ the strain tensor, λ_E, μ_E are the Lamé constants and δ the Kroneker delta. Repeated indices are summed. The magma chamber is described by an oblate spheroidal cavity with surface S in Cartesian coordinates $(x_j = x_1, x_2, x_3)$ with semi-major axis a and semi-minor axis c $(a \geq c)$

$$\frac{x_1^2 + x_2^2}{a^2} + \frac{x_3^2}{c^2} = 1. \tag{6}$$

On S we have an overpressure boundary condition

$$\sigma_{ij} n_i n_j = \Delta P, \tag{7}$$

where n is an outward unit normal vector. The free surface $x_3 = D$ is stress free, and stresses decay with distance from the chamber.

Cervelli (2013) provides an approximate analytic solution to the problem of a pressurized ellipsoidal inclusion in an elastic half space that matches boundary conditions on the chamber and free surface in successive higher order terms (McTigue, 1987; Segall, 2010), extending the results of Yang et al. (1988). Example von Mises stresses for an oblate chamber at relevant depths and overpressure for Mazama are contoured in Fig. 5.A, along with trajectories of least compressive principal deviatoric stresses projected onto the vertical medial plane of the chamber (black lines). Evidently only near the surface is there rotation of principal stresses out-of-plane. Opening mode cracks (such as dikes) propagate approximately perpendicular to these trajectories. Away from the chamber the direction of dike propagation (in the absence of other background stress) is vertical, but this example shows that near to the chamber (both below and above) significant reorientation of dikes may occur.

The Earth's free surface affects deviatoric stress magnitudes as well as orientations, becoming important as the lateral dimension of a magma chamber becomes similar to its depth (Supplementary Material Fig. S2). The free surface is ultimately responsible for generating stress concentrations that produce ring fractures and caldera collapse (Gudmundsson, 1998; Marti et al., 2008). As the chamber grows larger laterally, the free surface begins to project a larger capture zone at depth as the load better approximates a surface load (Karlstrom et al., 2009). Because estimates based on dissolved H_2O in melt inclusions place the top of the Mazama chamber at ~5 km with a thickness of perhaps several kilometers (Bacon et al., 1992; Mandeville et al., 2009), we can expect that free surface stress effects are non-negligible. Of course, the stress field below the chamber approaches that of the infinite space solution as depth increases (McTigue, 1987), and we use this fact to explore the role of extensional background stress on dike capture in the Supplementary Material.

It is also probable that the long eruptive history at Mazama resulted in warmed host rocks and viscoelastic host rocks surrounding the magma chamber. Viscoelastic effects promote the stability of magma chambers through relaxation of deviatoric chamber stresses that otherwise lead to failure (Dragoni and Magnanensi, 1989). The spatial extent and influence of viscoelastic host rocks depends on the enthalpy influx and thermal state of host rocks. Karlstrom et al. (2010) show that a stability criterion is the ratio of a chamber pressurization timescale $\tau_E \approx \Delta P V_{Ch}/EQ$ and relaxation timescale $\tau_{VE} \approx \mu_{Ch}/E$ (defining a Deborah number $\mathrm{De} = \tau_{VE}/\tau_E$). Here V_{Ch} is the chamber volume, Q the magma influx rate, E is Young's modulus of host rocks, and μ_{Ch} the viscosity of the shell. $\mathrm{De} \gg 1$ results in rapid pressurization and chamber failure, while for $\mathrm{De} \ll 1$ chambers do not pressurize but may freeze in time if there is insufficient magma influx. $\mathrm{De} \sim 1$ results in rapid chamber growth with melt influx and pressurization balanced by relaxation of host rock stress.

Using parameters appropriate for Mazama in the 20–30 ky preceding caldera collapse, Q = 1–15 km^3/ky, V_{Ch} = 100–500 km^3 chamber volume (spherical radius of 3–5 km based on caldera radius), E = 10 GPa, $\mu_{Ch} = 10^{16}$–10^{17} Pa s (we expect some prewarming of the mid to shallow crust due to the prior history of magma transport), and ΔP = 10–100 MPa, we find generally that τ_E and τ_{VE} do not differ by more than an order of magnitude.

3.2. Magma chamber–dike interactions

The source of overpressure in our model is recharge from rising dikes. Dikes are assumed highly pressurized, directed towards the magma chamber after encountering chamber deviatoric stress of sufficient magnitude (e.g., magma flows down pressure gradients, illustrated in Fig. 5). Such one way coupling is an upper bound on magmatic focusing, but provides a simple model for sourcing of magmas from a broad region at depth that scales with chamber size and pressure. We do not rule out the possibility that the Mazama vent distribution reflects a variety of focusing processes operating at different levels in the plumbing system. However, the presence of the caldera, along with petrologic (Section 2.1) and statistical (Section 2.2) evidence suggests that chamber effects may reasonably dominate. Deviatoric stress magnitude in host rocks falls off as ~1/distance^3 from a pressurized magma chamber. But the capture zone still extends up to 10–20 km from the chamber for large volume systems at reasonable overpressures, dominating edifice effects for large chambers (Karlstrom et al., 2009) and providing an upper crustal mechanism to mix dissimilar source magmas (e.g., Eichelberger, 1974).

Compositions of eruptive units leading up to CFE show evidence for two classes of magmas: those that represent relatively primitive magmas that ascended to the surface without significant differentiation during crustal storage (regional eruptions), and those that represent small-volume tapping of the growing centralized magma chamber (Mazama eruptions, Bacon and Lanphere, 2006). Both regional and Mazama eruptions migrate away from the eventual caldera center with regional eruptions outboard of Mazama eruptions (Fig. 2.B). The lensing model predicts that magma chamber growth is reflected at the surface as a growing zone of silence in which no regional eruptions occur, mirroring dike capture and stresses surrounding the chamber (Fig. 5.A), and Mazama eruptions that follow evolving stress trajectories to the surface. Grow-

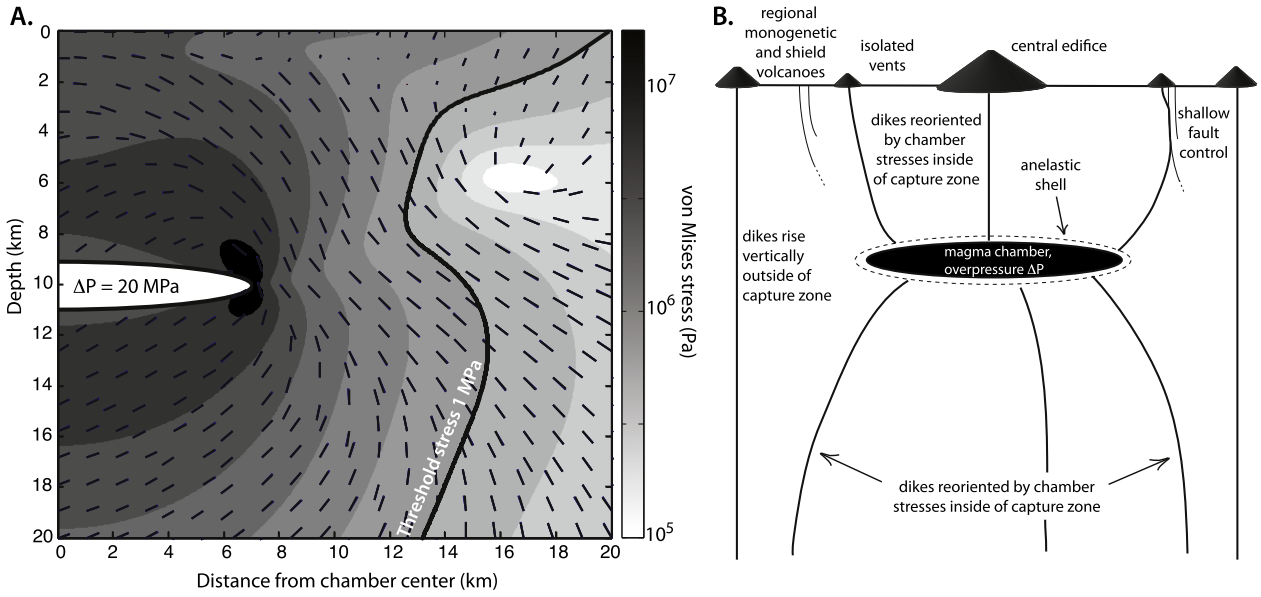

Fig. 5. A. Stress magnitudes (contoured) and least compressive principal deviatoric stress trajectories (black lines are vectors projected onto a vertical plane) around a pressurized magma chamber ($\Delta P = 20$ MPa, no extension) beneath a stress free surface. The thick 1 MPa contour is the modeled capture zone inside which dikes, propagating in planes perpendicular to the normal vectors plotted, could be affected by chamber stresses. **B.** Sketch of the Mazama plumbing system, showing dikes that escape chamber influence to erupt as regional volcanics, rising dikes focused towards the chamber to be trapped and Mazama eruptions that tap the reservoir, following chamber stresses and/or shallow faults to the surface. Dike trajectories in thin black lines here are schematic. Dashed line indicates a shell of anelastic wall rocks surrounding the chamber in which deviatoric stresses are relaxed.

ing stress influence determines the maximum lateral distance of Mazama-related eruptions from the center, which then mirrors the zone of silence for regional eruptions. Following large central vent eruptions that drain the chamber and release accumulated overpressure, both regional and Mazama eruptions could return to proximal areas as the effective chamber volume and deviatoric stresses are reduced.

Thus there is a positive feedback between recharge, pressurization, and magmatic lensing efficacy. A dike recharge event will increase stresses around the magma chamber at fixed volume, which will in turn enlarge the capture zone and cause increased influence on subsequent rising dikes. Chamber growth alone at fixed (even zero) pressure also matters, as capture zone size scales with chamber volume.

3.3. Magma chamber growth

Magma chamber pressurization with variable flux, extensional background stresses, and viscoelastic relaxation follows from three coupled ordinary differential equations that describe time evolution of chamber overpressure ΔP, chamber volume, V_{Ch} and magma influx rate Q to the chamber:

$$\frac{d\Delta P}{dt} = K\left(\frac{Q}{V_{Ch}} - \frac{\Delta P}{\mu_{Ch}}\right), \tag{8}$$

$$\frac{dV_{Ch}}{dt} = Q, \tag{9}$$

$$\frac{dQ}{dt} = \frac{d}{dt}(qA_{cap}) = A_{cap}\frac{dq}{dt} + q\left(\frac{dA_{cap}}{d\Delta P}\frac{d\Delta P}{dt} + \frac{dA_{cap}}{dV_{Ch}}\frac{dV_{Ch}}{dt}\right). \tag{10}$$

Here t is time, K is the bulk modulus of chamber material plus country rocks, and μ_{Ch} is wall rock viscosity. In general these equations contain additional contributions from pressure-volume accommodation due to extension $\dot{\epsilon}_{ext}$ (e.g., Jellinek and DePaolo, 2003), chamber heating/cooling and volatile exsolution that modifies the effective compressibility of the system and potential for failure through second boiling (e.g., Woods and Huppert, 2003; Fowler and Spera, 2008; Degruyter and Huber, 2014). The geologic tectonic extension rate $\dot{\epsilon}_{ext} \sim 10^{-8}$ yr^{-1} translates to 0.17 mm/yr averaged over the ~15 km E–W extent of volcanism (Bacon et al., 1999), negligible in influence for the range of fluxes and chamber sizes considered here. We thus focus primarily on the role of influx through Eq. (10). q is the vertical flux of magma from depth (in m/s, assumed an average rate over the Mazama region), and A_{cap} is the capture region over which magma is drawn toward the chamber at depth. Eq. (10) accounts for the possibility that A_{cap} may depend on chamber pressure and volume and that the source flux may be unsteady in time.

The detailed history of a magma storage zone through multiple recharge and eruptive events is complex. Relatively small volume eruptions that bear resemblance in composition to CFE magmas (Figs. 2, 6 and Supplementary Material) indicate that the chamber was tapped multiple times leading up to the caldera forming eruption (Bacon and Lanphere, 2006). We do not attempt to model this eruptive history explicitly, assuming that small eruptions do not significantly affect longer term evolution. This is a requirement for net growth of the reservoir.

Instead, we model time-averaged Mazama magma chamber growth following a rapid increase in melt influx q to the Mazama plumbing system 40–50 ky before the CFE with two mechanical end member growth scenarios. Model 1 in what follows assumes that viscoelastic relaxation of stresses by creeping wall rocks is rapid so there is no appreciable overpressure in the chamber during growth (Jellinek and DePaolo, 2003). The chamber grows by trapping magmas that rise beneath it as a "density filter" (e.g., Walker, 1974; Smith, 1979; Shaw, 1985). Model 2 in what follows assumes that recharge and pressurization dominate expansion so an elastic stress field is maintained in wall rocks. In this case the chamber is assumed buffered towards a constant overpressure during growth, and capture of rising mafic magmas reflects dike reorientation and capture by chamber stresses as well as chamber growth.

Models 1 and 2 are distinct limits to Eqs. (8)–(10), both of which involve $d\Delta P/dt \to 0$ (more detailed discussion in the Supplementary Material). Model 1 assumes that the Deborah number

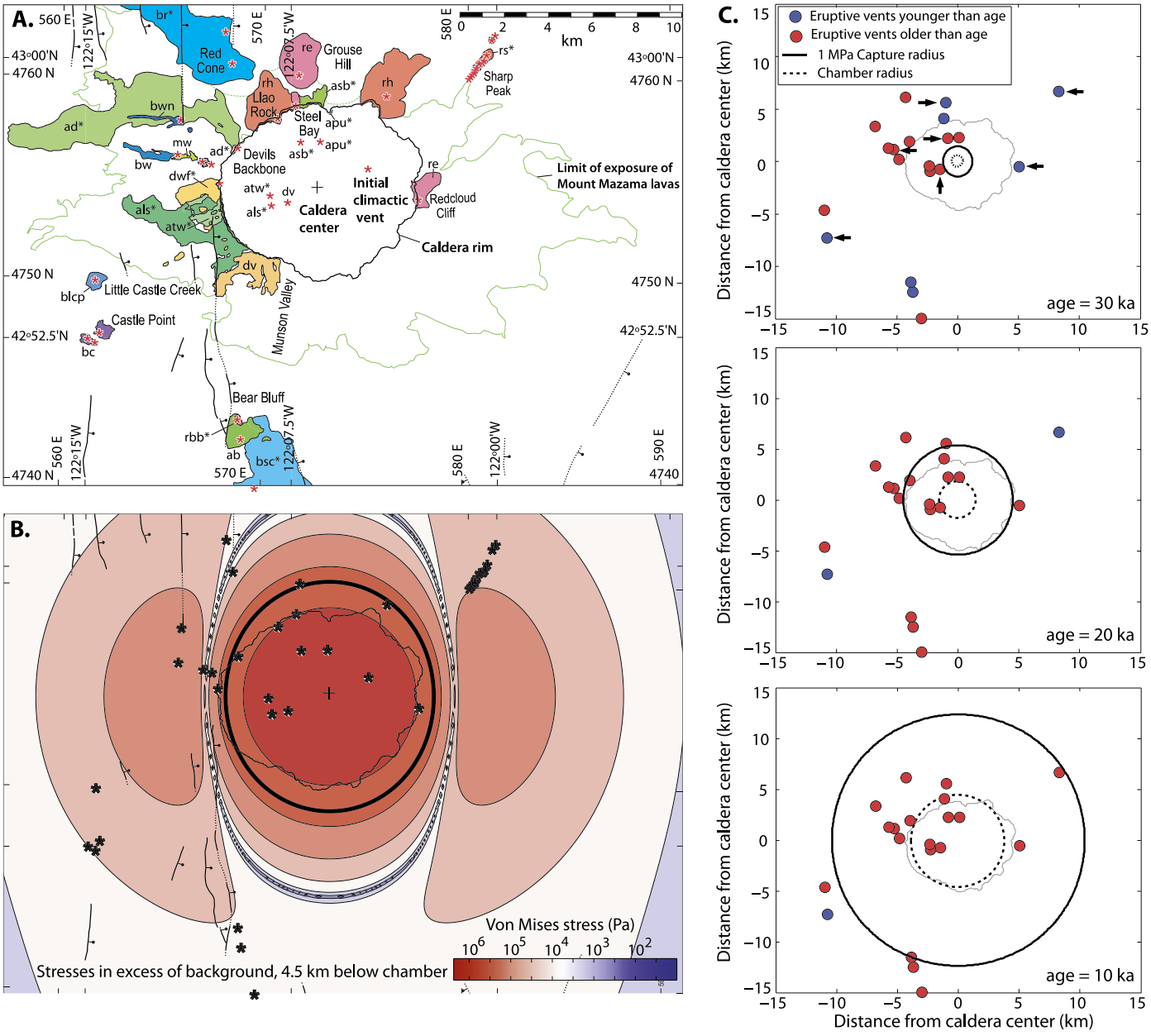

Fig. 6. A. Geologic map of the Mazama region, modified after Bacon and Lanphere (2006), showing mapped eruptive units (colored) and vents (asterisks) younger than 55 ka as well as the caldera rim and regional faults. **B.** Example von Mises stress field in excess of regional extensional stress (Supplementary Material) at maximum capture zone 4.5 km below the medial plane of an oblate spheroidal chamber with $a = 5$ km and $\sigma_{ext} = 1$ MPa. Overpressure $\Delta P = 40$ MPa, color in log scale with thick black contour the 1 MPa capture radius. Background vents, faults and caldera rim as in part A. **C.** Map view time series illustrating the expansion of the capture zone during chamber growth (Model 2 with parameters as in B). Plotted in 10 ky increments starting at 30 ka are primary vent locations <55 ka as in Supplementary Material (symbol color indicates whether a given eruption has occurred at given time stamp), magma chamber radius and capture radius. Arrows in top panel indicate the modeled vent locations in Table 1. (For interpretation of the references to color in this figure legend, the reader is referred to the web version of this article.)

$\mathrm{De} = \tau_{VE}/\tau_E \ll 1$ (again noting that we neglect thermal effects here). In this case $\Delta P \to 0$ on timescale τ_{VE}, while the chamber grows as $V_{Ch} = Q\,t + V_{Ch}$ $(t = 0)$. The capture zone for dikes is then the footprint of the chamber (the classic density filter model for silicic systems invokes this implicitly). Model 2 takes the case De ~1, and assumes a prolonged time period in which chamber pressure is buffered at ΔP_{crit}. The duration of pressure buffering scales with the effective compressibility of the system but can be up to $10^4 \times \tau_E$ (Supplementary Material). The regime $\mathrm{De} \gg 1$ results in pressurization that dominates growth, so that overpressure through Eq. (8) exponentially increases past the critical overpressure ΔP_{crit} on the elastic timescale τ_E. The chamber is unstable in this regime.

Thermal arguments in Section 3.1 suggest that, leading up to CFE, Mazama may have been in a regime of De ~ 1. Model 2 requires that, even if rapid pressurization and failure of the chamber occurs (the $\mathrm{De} \gg 1$ scenario), time averaged chamber pressure is buffered towards ΔP_{crit}. Long-term volumetric growth of the chamber is then mostly unaffected by small volume eruptions that may tap the reservoir. A finite thickness low viscosity shell (not a feature of the present simplified model, which assumes constant wall rock viscosity) is one way to produce this behavior (Karlstrom et al., 2010). We recognize that the pressure at which magma chambers can be buffered could also vary in time as the chamber grows and wall rock viscosity evolves on a diffusion timescale (Jellinek and DePaolo, 2003), however we assume that it is con-

Table 1
Eruptive vents forming closest approach to climactic collapse center for regional and Mazama fits, along with mean and standard error of all model runs that totaled less than 3 km total misfit. Model 1 has sample number $n = 32$ and Model 2 has $n = 172$ for calculating mean and standard deviation. Further information on these eruptions may be found in the Supplementary Material. Eruption asb labeled 'Reg*' was sourced from the Mazama chamber but is used to provide an anchor to start the regional vent fitting.

Age (ka)	UTM Easting NAD 1927	UTM Northing NAD 1927	Distance from caldera center (km)	Azimuth (degrees from E)	Unit label (Bacon, 2008)	Regional or Mazama fitting	Model 1 error (km) mean ± std	Model 2 error (km) mean ± std
10	561960	4747260	12.96	−145.8	bc	Reg	1.4 ± 0.4	−0.4 ± 1.5
35	566700	4755800	5.82	167.6	bw	Reg	1.5 ± 0.4	1.4 ± 0.6
43	571840	4756770	2.4	167.6	asb	Reg*	0.3 ± 0.6	−0.1 ± 0.6
18	580990	4761220	10.7	138.8	rs	Maz	2.5 ± 0.1	0.5 ± 1.5
27	577700	4754020	5.0	−6.0	re	Maz	0.5 ± 0.2	0.3 ± 0.7
27	571560	4758630	4.2	105.2	re	Maz	−0.3 ± 0.2	−0.8 ± 0.7
35	571210	4753780	1.7	−152.5	dv	Maz	0.2 ± 0.2	−0.2 ± 0.6

stant here. Models 1 and 2 both allow for a positive feedback between influx and growth, while Model 2 exhibits the additional feedback that the dike capture zone scales with chamber size even at fixed pressure.

We neglect time variation in the source flux of magma apart from a single step increase that begins the period of chamber growth. Thus $dq/dt = 0$ in Eq. (10), and the time evolution equations, reduce to

$$\frac{dV_{Ch}}{dt} = Q \tag{11}$$

$$\frac{dQ}{dt} = q\frac{dA_{cap}}{dV_{Ch}}\frac{dV_{Ch}}{dt} \tag{12}$$

where A_{cap} is set by the maximum footprint under the chamber in which deviatoric stresses measured by the von Mises stress σ_{VM} exceed a threshold stress σ_{Crit}

$$\sigma_{VM} = 3\sqrt{J_2} = \sigma_{Crit}. \tag{13}$$

We assume that rising dikes have a time averaged constant influx throughout the Mazama region ($q = const$), consistent with the statistically random temporal and clustered spatial distribution of vents (Fig. 4).

If extension is present the capture footprint is elongated perpendicular to the extension direction, and axisymmetric otherwise (illustration of von Mises stresses and capture zone in the presence of extension shown in Fig. 6.B, further details in the Supplementary Material). J_2 is the second deviatoric stress invariant, and although poorly constrained we assume $\sigma_{Crit} = 1$ MPa (Rubin, 1995; Karlstrom et al., 2009). If overpressures are small or zero, A_{cap} reduces to the chamber area and $dA_{cap}/dV_{Ch} = 3/4c$. Model 1 uses $\Delta P = 0$ while Model 2 takes constant $\Delta P > 0$. Scalar metrics of deviatoric stress other than von Mises such as a Coulomb or least principal deviatoric stress do not result in significantly different predictions of chamber stress magnitudes (Karlstrom et al., 2012), so we use von Mises for simplicity.

4. Simulation procedure and results

We model the closest approaching vents to the caldera center until the CFE at 7.7 ka and the two (possibly related) eruptions immediately preceding (map unit rh, Fig. 6). For regional eruptions, dikes not captured by the magma chamber rise freely to the surface without chamber influence (Fig. 5), resulting in monogenetic cones surrounding the central vent zone. For each simulation we fit, in a least squares sense, the evolving extent of the capture zone defined by Eq. (13) (Model 2) or chamber radius (Model 1) to the distance, azimuth, and time of nearest surface eruptions. No other vent locations are modeled. We fit Mazama eruptions and regional eruptions separately, consistent with the different depths of origin (Table 1, additional discussion in Supplementary Material). This provides some measure of uncertainty in parameter estimations in light of simplifying model assumptions. The governing differential–algebraic equations (11) and (12) are solved with a 4th order Runge–Kutta method beginning 30–55 ky before the CFE.

The complete set of eruptions younger than 55 ka (including eruptions not fit) is shown in Fig. 6.A along with mapped flow units. Fig. 6.C shows an example Model 2 fit in map view, plotting the maximum extent of the capture zone (used to fit Mazama eruptions in this case) and the chamber radius along with surface eruptions. Note that the depth at which the von Mises stresses are evaluated in Fig. 6.C varies since the maximum extent of lateral capture zone scales with chamber size (contoured stresses in Fig. 5).

A number of model input parameters are uncertain: chamber overpressure (Model 1 versus Model 2), initial time (onset of chamber growth), extensional stress, chamber geometry, and initial chamber size. We assume that initial size is uniform (0.5 km semi-major axis chamber centered under the caldera). Initial overpressure is zero for model 1 and finite (fixed in time) for Model 2. Melt influx is left as a free parameter, with constraints from petrologic modeling (Section 2.1) used to compare and evaluate models.

We perform simulations that realize a coarse grid search over the remaining parameter space to find parameters that best fit eruption times and locations. For Model 2 we vary constant influx $Q = 1$–100 km^3/ky, averaging over the area of vents for regional eruptions. We assume a circular input area with radius slightly beyond the farthest eruption from the CFE reservoir center in the last 55 ky (13 km) or the last 400 ky (20 km), which gives model influx in the range of 8×10^{-4} to 9×10^{-2} m^3/m^2/yr. For Model 1, we experiment with a larger range of input flux to obtain good fits. Magma chamber overpressure we vary between 1 MPa and 85 MPa, spanning a variety of constraints on this failure criterion (Rubin, 1995; Grosfils, 2007; Currenti et al., 2010; Gudmundsson, 2006). We test three aspect ratios for the oblate spheroid: $a/c = 2, 5$ and 10 for both models, and experiment with non-zero extensional background stress (Supplementary Material).

We define goodness of fit in terms of total summed difference between vent locations and model chamber radius (Model 1) or capture radius (Model 2), defining a summed absolute value of error less than 4 km (less than 4 km total difference between vent locations and model) as "good fit." Example models are illustrated in Fig. 7, with good fits as a function of model parameters in Figs. 8 and 9. Boxed symbols are the examples plotted on eruption data in Fig. 7.

Between classes of vents we find different best fitting durations of chamber growth, 32 ky for Mazama vents and 46 ky for regional vents with good fits for both (Fig. 7). We use these as minimum and maximum bounds for the onset time of increased melt influx that drives chamber growth. For Model 2, good fits trade off between assumed influx and overpressure, a non-uniqueness common to elastic inversions (Segall, 2010). Models that fit the

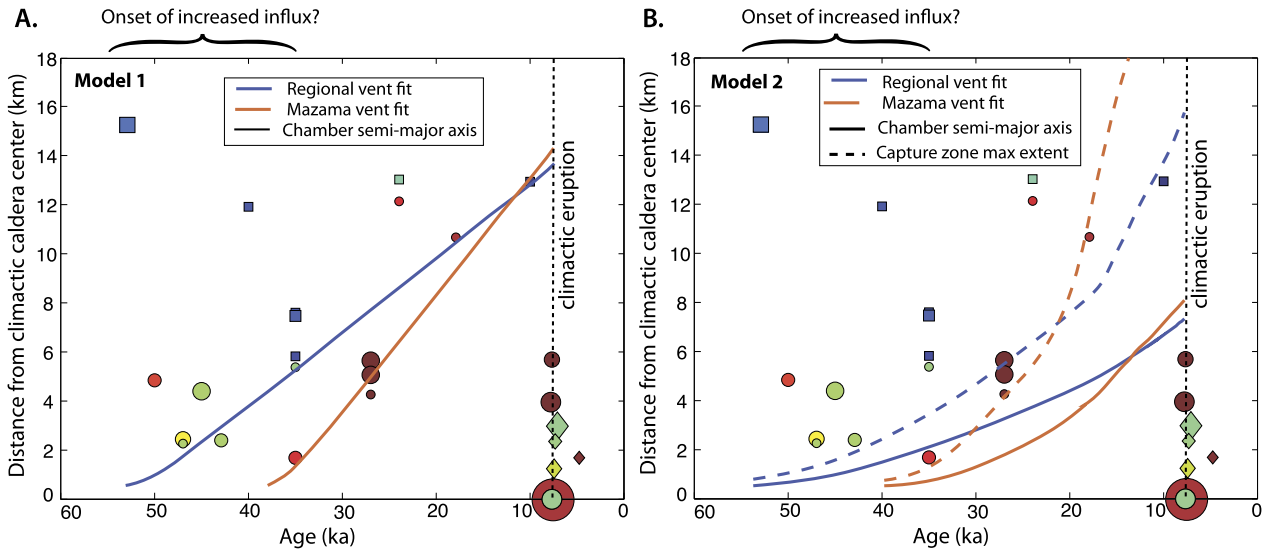

Fig. 7. A. Mazama eruptive history since 55 ka showing example model fits for regional (blue solid lines indicate chamber semi-major axis) and Mazama (orange lines) vents for Model 1. $Q = 57.5$ km^3/ky for Mazama vents and $Q = 85.9$ km^3/ky for regional vents. **B.** Model 2 fits, with dashed lines now illustrating the capture radius defined by von Mises stresses in excess of 1 MPa and solid lines the chamber semi-major axis. $Q = 18.25$ km^3/ky and $\Delta P = 10.0$ MPa for regional vents, $Q = 12.8$ km^3/ky and $\Delta P = 28.9$ MPa for Mazama vents. Oblate spheroidal geometry with $a/c = 10$ in both cases, with no regional extension. Eruption symbol color and size as in Fig. 2.B. (For interpretation of the references to color in this figure legend, the reader is referred to the web version of this article.)

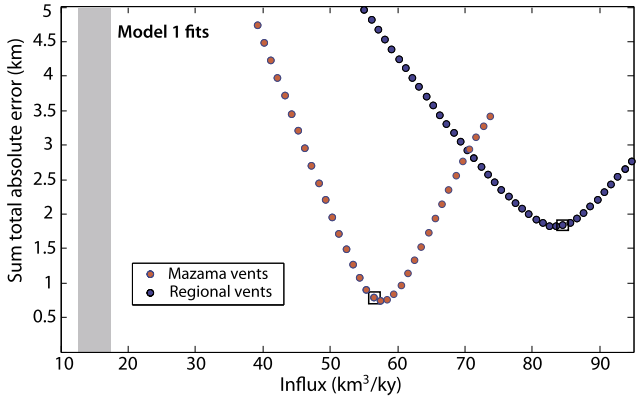

Fig. 8. Model 1 fits for regional (blue symbols) and Mazama (orange symbols) vents. Chamber overpressure is zero in this model. Gray bar is estimated melt flux to the Mazama region, while boxes indicate the specific simulations plotted in Fig. 7.A. (For interpretation of the references to color in this figure legend, the reader is referred to the web version of this article.)

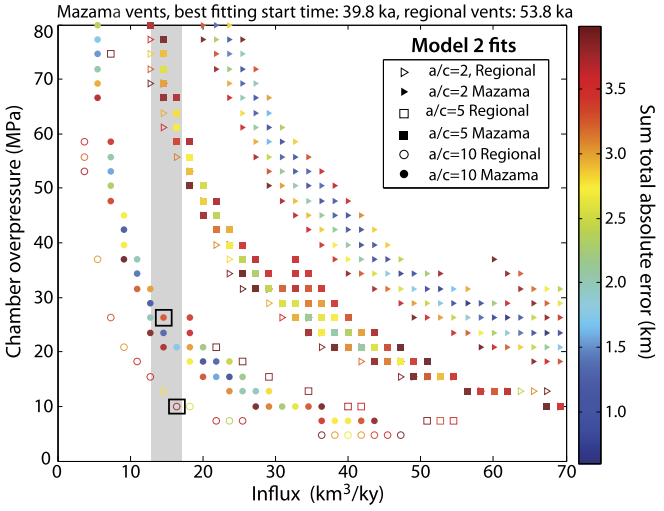

Fig. 9. Parameter space of Model 2 realizations showing fits to regional (open symbols) and Mazama (filled symbols) vents colored by total error. Symbols shapes correspond to different aspect ratios (a/c) of the oblate chamber centered at 10 km depth. Gray bar is the influx constrained by eruptive history corrected for fractional crystallization (Fig. 3), with boxes showing the specific simulations plotted in Fig. 7.B. Top label indicates best fitting modeled onset of chamber growth for regional versus Mazama vents. (For interpretation of the references to color in this figure legend, the reader is referred to the web version of this article.)

$\sim$15 km^3/ky influx constraints have overpressures that range from 10 to 85 MPa depending on regional/Mazama fit and geometry. Lowest overpressures are for a chamber aspect ratio of $a/c = 10$, for which differences between fitted regional and Mazama eruptions result in a predicted overpressure range of 10–30 MPa (Fig. 9). For Model 1, we find good fits for the $a/c = 10$ oblate spheroid in the range of 40–100 km^3/ky (Fig. 8). Model fits for lower aspect ratio chambers require much greater influx, and we do not present the results.

5. Discussion

Caldera-forming eruptions are rare, catastrophic events that are part of the life cycle at many volcanic centers, requiring a shallow and often quite large magma chamber at depth (e.g., Lipman, 1984). Our results suggest that the space–time distribution of regional and Mazama related eruptions, combined with a detailed record of eruptive volumes and compositions, provide quantitative insight into the evolving silicic magma reservoir that led to the climactic caldera-forming eruption at ca. 7.7 ka. There is ample evidence for a centralized magma storage zone that produced smaller volume silica eruptions through much of the Mazama eruptive history (e.g., the dacite of Pumice Castle at $\sim$70 ka, Bacon and Lanphere, 2006).

We hypothesize that a rapid increase in melt influx beginning between 40–50 ka triggered an episode of chamber growth and magma differentiation that ultimately led to caldera collapse. While we do not speculate on the cause for such an increase in melt influx here, one possibility is the triggering of enhanced deep melt production by ice unloading (e.g., Bacon and Lanphere, 2006; Watt et al., 2013) during MIS 3, $\leq$60 ka (Bassinot et al., 1994). However, thicknesses of ice-bounded lava flows that date from MIS 4 suggest ice was on the order of 100 m thick, so one must appeal to a small amplitude change in load upon deglaciation to

explain our results. After caldera formation, any remaining reservoir is less able to capture and retain rising dikes so residual stored magma or deep recharge events may rise to the surface near the climactic eruptive center to produce the post-caldera eruption distribution (Fig. 2.B). Such a sequence of small volume mafic eruptions appearing near or within a recently formed caldera is commonly observed (e.g., Stehn, 1929; Kamata, 1989; Marti and Gudmundsson, 2000).

To test this hypothesis, we have developed a model for the Mazama plumbing system based on two end member representations of magma chamber growth. We consider a model in which elastic deviatoric stresses maintained outside of an anelastic shell (Model 2) focus rising dikes towards the chamber, and a model in which the chamber grows in an effectively viscous crust (Model 1, the classic density filter model for silicic centers, e.g., Walker, 1974) where recharge is limited to the growing footprint of the chamber. Both representations provide good fits to eruptive vent locations through time (Figs. 8–9). Although Model 2 fits influx estimates better than Model 1, the discrepancy in matching influx for Model 1 is a factor of 3–6 for oblate chamber geometries and should be considered within the range of uncertainty of our influx estimates. Indeed, because our purely fractional crystallization based estimates of influx are likely a lower bound, it is possible that the true influx was higher. However, combined with the large lateral dimension of Model 1 chambers (∼13 km to match vent locations, ∼10 km larger than the initial caldera collapse radius), we favor Model 2 as the more plausible scenario for Mazama chamber growth.

Best fits for Model 2 trade off influx inversely with overpressure. Overpressures between 10–85 MPa match influx estimates derived using erupted volumes corrected for fractional crystallization (∼15 km^3/ky). Best fitting models for a highly oblate chamber at the lower end of these overpressures (10–30 MPa) would seem to be most consistent with low pressure laboratory estimates of maximum overpressure (Gudmundsson, 2012). Onset time of chamber growth is coarsely estimated to be within 40–50 ky prior to the climactic eruption based on separate fits to regional and Mazama eruptions, and extensional stresses are not well constrained (Supplementary Material).

Chamber semi-major axis at the time of CFE is a strong function of assumed geometry, varying in best fitting models between 3.5–12 km for Model 2, and ∼13 km for Model 1 (required uniformly to match vent locations). Model 2 realizations that match estimated influx predict final chamber radius between 4.5–8.5 km (Fig. 7, Supplementary Material). These estimates are all larger than the ∼2.5 km radius of caldera subsidence at the time of the climactic eruption (Suzuki-Kamata et al., 1993). However, caldera size may reflect chamber size only for crystal poor caldera-forming eruptions due to syneruptive rheological phase transitions within crystal rich reservoirs (Karlstrom et al., 2012). The progression of most climactic eruptions towards extremely crystal rich magmas in the later stages of the caldera forming event (up to 50–66% crystals) with individual blocks of granodiorite wall rock reaching meters in size (some partially melted, along with lithic clasts from the edifice, Bacon, 1983, 1992) suggests that the climactic caldera radius could well have been smaller than the chamber radius.

Including the effects of edifice loading (e.g., Pinel and Jaupart, 2000), background stress and layered media (Gudmundsson, 2006) on failure criteria, and coupling to thermal evolution (e.g., de Silva and Gregg, 2014), may help to better constrain these model parameters. Although faulting has clearly affected lateral transport and vent locations for some Mazama eruptions (for example the far-flung rhyodacite of Bear Bluff, Fig. 6), the depth extent of such structural control on dike pathways must compete with dynamic stresses within the magma transport system itself and should be limited to the shallow subsurface. Perhaps more significantly, the co-evolving reservoir/wall rock system surely influences the size, timing and compositions of small volume eruptions. Future work modeling the occurrence of small volume eruptions from the Mazama chamber (rather than focusing on background chamber growth as we have done) could yield significant insight into controls on eruption timing, and the ultimate trigger for CFE.

Focusing of dikes by a growing magma chamber provides a plausible mechanism for clustering of eruptions around the Mazama center that is consistent with geologic constraints. Similar dike focusing processes could play a role in the along-arc localization of other long-lived volcanic centers (e.g., Hildreth, 2007) above more spatially continuous subduction-induced mantle melting generally (Karlstrom et al., 2009). The average background melt influx in the Mazama region estimated from eruption volumes preceding our assumed onset of chamber growth at ∼35 ka is 0.74 km^3/ky (Supplementary Material). This falls into the range of estimated lower crustal influx at other arc plutonic and silicic caldera-forming systems (White et al., 2006), consistent with constraints from thermal models (Annen, 2009).

We do not model thermal effects explicitly here, however transient melt flux increased above these background levels may be required to build reservoirs with any significant melt fraction in the cool shallow crust. Average Mazama melt influx increased roughly an order of magnitude above background after 35 ka and perhaps earlier (6.4 km^3/ky averaged over 30 ky or 14–15 km^3/ky using just flux from CFE), less than that estimated based on purely thermal models to generate a high melt fraction reservoir at 10 km depth in a normal geothermal gradient (Schöpa and Annen, 2013). This suggests prewarmed rocks at the ∼10 km reservoir depth, plausible given the >350 ky of prior crustal magma transport at Mazama. Such crustal warming may play a role in transitions between central edifice dominated volcanic centers (small shallow reservoirs, frequent and spatially distributed monogenetic eruptions) to caldera formation (large shallow reservoirs, suppressed monogenetic eruptions) in arc settings generally (e.g., Smith, 1979; Hildreth, 1981).

Acknowledgements

We thank editor Tim Elliott, Manuel Nathenson, Shanaka L. de Silva, and two anonymous reviewers for constructive comments that improved the manuscript. L.K. acknowledges support from NSF postdoctoral fellowship EAR1143623.

Appendix A. Supplementary material

Supplementary material related to this article can be found online at http://dx.doi.org/10.1016/j.epsl.2014.12.001.

References

Anderson, K., Segall, P., 2011. Physics-based models of ground deformation and extrusion rate at effusively erupting volcanoes. J. Geophys. Res. 116 (B07204).
Annen, C., 2009. From plutons to magma chambers: thermal constraints on the accumulation of eruptible silicic magma in the upper crust. Earth Planet. Sci. Lett. 284, 409–416.
Bacon, C.R., 1983. Eruptive history of Mount Mazama and Crater Lake Caldera, Cascade Range, USA. J. Volcanol. Geotherm. Res. 18, 57–115.
Bacon, C.R., 1992. Partially melted granodiorite and related rocks ejected from Crater Lake caldera, Oregon. Trans. R. Soc. Edinb. Earth Sci. 83, 27–47.
Bacon, C.R., 2008. Geologic map of Mount Mazama and Crater Lake Caldera, Oregon. U.S. Geological Survey Scientific Investigations Map 2832.
Bacon, C.R., Druitt, T.H., 1988. Compositional evolution of the zoned calcalkaline magma chamber of Mount Mazama, Crater Lake, Oregon. Contrib. Mineral. Petrol. 98, 224–256.
Bacon, C.R., Lanphere, M.A., 2006. Eruptive history and geochronology of Mount Mazama and the Crater Lake region, Oregon. Geol. Soc. Am. Bull. 118 (11), 1331.
Bacon, C.R., Newman, S., Stolper, E., 1992. CO_2, Cl, and F in melt inclusions in phenocrysts from three Holocene explosive eruptions, Crater Lake, Oregon. Am. Mineral. 77, 1021–1030.

Bacon, C.R., Gunn, S.H., Lanphere, M.A., Wooden, J.L., 1994. Multiple isotopic components in Quaternary volcanic rocks of the Cascade arc near Crater Lake, Oregon. J. Petrol. 35, 1521–1556.
Bacon, C.R., Lanphere, M.A., Champion, D.E., 1999. Late quaternary slip rate and seismic hazards of the West Klamath Lake fault zone near Crater Lake, Oregon Cascades. Geology 1, 43–46.
Baloga, S.M., Glaze, L.S., Bruno, B.C., 2007. Nearest neighbor analysis of small features on Mars: applications to tumuli and rootless cones. J. Geophys. Res. 112 (E03002).
Bassinot, F.C., Labeyrie, L.D., Vincent, E., Quidelleur, X., Shackleton, N.J., Lancelot, Y., 1994. The astronomical theory of climate and the age of the Brunhes–Matuyama magnetic reversal. Earth Planet. Sci. Lett. 126, 91–108.
Cervelli, P.F., 2013. Analytical expressions for deformation from an arbitrarilly oriented spheroid in a half-space. EOS Transactions of the American Geophysical Union abstract V44C-06, http://volcanoes.usgs.gov/software/spheroid/.
Coleman, D.S., Gray, W., Glazner, A.F., 2004. Rethinking the emplacement and evolution of zoned plutons: geochronologic for incremental assembly of the Tuolumne Intrusive Suite, California. Geology 32 (5), 433–436. http://dx.doi.org/10.1130/G20220.1.
Connor, C.B., Hill, B.E., 1995. Three nonhomogeneous Poisson models for the probability of basaltic volcanism: application to the Yucca Mountain region, Nevada. J. Geophys. Res. 100 (B6), 10107–10126.
Cox, D.R., Lewis, P.A.W., 1966. The Statistical Analysis of Series of Events. Methuen, New York.
Currenti, G., Williams, C.A., 2014. Numerical modeling of deformation and stress fields around a magma chamber: constraints on failure conditions and rheology. Phys. Earth Planet. Inter. 226, 14–27.
Currenti, G., Bonaccorso, A., del Negro, C., Scandura, D., Boschi, E., 2010. Elasto-plastic modeling of volcano ground deformation. Earth Planet. Sci. Lett. 296, 311–318.
de Silva, S.L., 1989. The Altiplano–Puna complex of the central Andes. Geology 17, 1102–1106.
de Silva, S.L., Gregg, P.M., 2014. Thermomechanical feedbacks in magmatic systems: implications for growth, longevity, and evolution of caldera-forming magma reservoirs and their supereruptions. J. Volcanol. Geotherm. Res. 282, 77–91.
Degruyter, W., Huber, C., 2014. A model for eruption frequency of upper crustal silicic magma chambers. Earth Planet. Sci. Lett. 403, 117–130.
Dragoni, M., Magnanensi, C., 1989. Displacement and stress produced by a pressurized, spherical magma chamber, surrounded by a viscoelastic shell. Phys. Earth Planet. Inter. 56, 316–328.
Dufek, J., Huber, C., Karlstrom, L., 2013. Magma chamber dynamics and thermodynamics. In: Fagents, S., Gregg, T., Lopez, R. (Eds.), Modeling Volcanic Processes: The Physics and Mathematics of Volcanism. Cambridge University Press.
Eichelberger, J.C., 1974. Magma contamination within the volcanic pile. Geology 2, 29–33.
Fowler, S.J., Spera, F.J., 2008. Phase equilibria trigger for explosive volcanic eruptions. Geophys. Res. Lett. 35 (L08309). http://dx.doi.org/10.1029/2008GL033665.
Grosfils, E.B., 2007. Magma reservoir failure on the terrestrial planets: assesing the importance of gravitational loading in simple elastic models. J. Volcanol. Geotherm. Res. 166, 47–75.
Gualda, C., Ghiorso, M.S., Lemons, R.V., Carley, T.L., 2012. Rhyolite-MELTS: a modified calibration of MELTS optimized for silica-rich, fluid-bearing magmatic systems. J. Petrol. 53 (5), 875–890.
Gudmundsson, A., 1998. Formation and development of normal-fault calderas and the initiation of large explosive eruptions. Bull. Volcanol. 60, 160–170.
Gudmundsson, A., 2006. How local stresses control magma-chamber ruptures, dyke injections, and eruptions in composite volcanoes. Earth-Sci. Rev. 79, 1–31.
Gudmundsson, A., 2012. Magma chambers: formation, local stresses, excess pressures, and compartments. J. Volcanol. Geotherm. Res. 237–238, 19–41.
Hildreth, W., 1981. Gradients in silicic magma chambers: implications for lithospheric magmatism. J. Geophys. Res. 86, 10153–10192.
Hildreth, W., 2007. Quaternary magmatism in the Cascades – geologic perspectives. Professional Paper 1744. US Geological Survey. http://pubs.usgs.gov/pp/pp1744/.
Jellinek, A.M., DePaolo, D.J., 2003. A model for the origin of large silicic magma chambers: precursors of caldera-forming eruptions. Bull. Volcanol. 65, 363–381. http://dx.doi.org/10.1007/s0045-003-0277-y.
Kamata, H., 1989. Shishimuta caldera, the buried source of the Yabakei pyroclastic flow in the Hohi volcanic zone, Japan. Bull. Volcanol. 51, 41–50.
Karlstrom, L., Dufek, J., Manga, M., 2009. Organization of volcanic plumbing through magmatic lensing by magma chambers and volcanic edifices. J. Geophys. Res. 114 (B10304). http://dx.doi.org/10.1029/2009JB006339.
Karlstrom, L., Dufek, J., Manga, M., 2010. Magma chamber stability in arc and continental crust. J. Volcanol. Geotherm. Res. 190, 249–270.
Karlstrom, L., Rudolph, M.L., Manga, M., 2012. Caldera size modulated by the yield stress within a crystal-rich magma reservoir. Nat. Geosci. 5, 402–405.
Lipman, P.W., 1984. The roots of ash flow calderas in western North America: windows into the tops of granitic batholiths. J. Geophys. Res. 89 (B10), 8801–8841.
Mandeville, C.W., Webster, J.D., Tappen, C., Taylor, B.E., Timbal, A., Sasaki, A., Hauri, E., Bacon, C.R., 2009. Stable isotope and petrologic evidence for open-system degassing during the climactic and pre-climactic eruptions of Mt. Mazama, Crater Lake, Oregon. Geochim. Cosmochim. Acta 73, 2978–3012.
Marsh, B.D., Carmichael, I.S., 1974. Benioff-zone magmatism. J. Geophys. Res. 79 (8), 1196–1206.
Marti, J., Gudmundsson, A., 2000. The Las Cañadas caldera (Terife, Canary Islands): an overlapping collapse caldera generated magma-chamber migration. J. Volcanol. Geotherm. Res. 103, 161–173.
Marti, J., Geyer, A., Folch, A., Gottsmann, J., 2008. A review on collapse caldera modelling. In: Gottsmann, J., Marti, J. (Eds.), Developments in Volcanology, vol. 10. Elsevier, pp. 233–283, Chapter 6.
Marzocchi, W., Bebbington, M.S., 2012. Probabilistic eruption forecasting at short and long time scales. Bull. Volcanol. 74 (8), 1777–1805.
Marzocchi, W., Zaccarelli, L., 2006. A quantitative model for the time-size distribution of eruptions. J. Geophys. Res. 111 (B4).
McTigue, D.F., 1987. Elastic stress and deformation near a finite spherical magma body – resolution of the point-source paradox. J. Geophys. Res. 92 (B12), 12931–12940.
Muller, J.R., Ito, G., Martel, S.J., 2001. Effects of volcano loading on dike propagation in an elastic half-space. J. Geophys. Res. 106 (B6), 11101–11113.
Nathenson, M., Clynne, M.A., Muffler, L.J.P., 2012. Eruption probabilities for the Lassen volcanic center and regional volcanism, northern California, and probabilities for large explosive eruptions in the cascade range. U.S. Geological Survey Scientific Investigations Report 2012-5176-B, p. 23.
Olson, P., Singer, H., 1985. Creeping plumes. J. Fluid Mech. 158, 511–531.
Pinel, V., Jaupart, C., 2000. The effect of edifice load on magma ascent beneath a volcano. Philos. Trans. R. Soc. Lond. A 358, 1515–1532.
Poland, M.P., Miklius, A., Sutton, A.J., Thornber, C.R., 2012. A mantle-driven surge in magma supply to Kilauea Volcano during 2003–2007. Nat. Geosci. 5, 295–300.
Rubin, A.M., 1995. Propagation of magma-filled cracks. Annu. Rev. Earth Planet. Sci. 23, 287–336.
Schöpa, A., Annen, C., 2013. The effects of magma flux variations on the formation and lifetime of large silicic magma chambers. J. Geophys. Res. 118, 1–17.
Segall, P., 2010. Earthquake and Volcano Deformation. Princeton University Press, Princeton, New Jersey.
Shaw, H.R., 1985. Links between magma-tectonic rate balances, plutonism, and volcanism. J. Geophys. Res. 90 (B13), 11275–11288.
Siebert, L., Simkin, T., Kimberly, P., 2011. Volcanoes of the World. University of California Press.
Smith, R.L., 1979. Ash-flow magmatism. In: Geological Society of America Special Paper, vol. 180, pp. 5–27.
Smith, R.L., Shaw, H.R., 1975. Igneous-related geothermal systems. In: U.S. Geological Survey Circular, vol. 726, pp. 58–83.
Stehn, C.E., 1929. The geology and volcanism of the Krakatau group. In: Proceedings of the 4th Pacific Science Congress. Batavia, pp. 1–55.
Suzuki-Kamata, K., Kamata, H., Bacon, C.R., 1993. Evolution of the caldera-forming eruption at Crater Lake, Oregon, indicated by component analysis of lithic fragments. J. Geophys. Res. 98, 14059–14074.
Wadge, G., Cross, A., 1989. Identification and analysis of the alignments of point-like features in remotely-sensed imagery: volcanic cones in the Pinacate volcanic field, Mexico. Int. J. Remote Sens. 10, 455–474.
Walker, G.P.L., 1974. Eruptive mechanisms in Iceland. In: Geodynamics of Iceland and the North Atlantic area. D Reidel Publishing Company, Dordrecht–Holland, pp. 189–201.
Watt, S.F.L., Pyle, D.M., Mather, T.A., 2013. The volcanic response to deglaciation: evidence from glaciated arcs and a reassessment of global eruption records. Earth-Sci. Rev. 122, 77–102.
White, S.M., Crisp, J.A., Spera, F.J., 2006. Long-term volumetric eruption rates and magma budgets. Geochem. Geophys. Geosyst. 7 (3).
Woods, A.W., Huppert, H.E., 2003. On magma chamber evolution during slow effusive eruptions. J. Geophys. Res. 108 (B8).
Wright, H.M.N., Bacon, C.R., Vazquez, J.A., Sisson, T.W., 2012. Sixty thousand years of magmatic volatile history before the caldera-forming eruption of Mount Mazama, Crater Lake, Oregon. Contrib. Mineral. Petrol. 164, 1027–1052.
Yang, X.-M., Davis, P.M., Dietrich, J.H., 1988. Deformation from inflation of a dipping finite prolate spheroid in an elastic half-space as a model for volcanic stressing. J. Geophys. Res. 93 (B5), 4249–4257.
Zak, J., Paterson, S.R., 2005. Characteristics of internal contacts in the Tuolumne Batholith, central Sierra Nevada, California (USA): implications for episodic emplacement and physical processes in a continental arc magma chamber. Geol. Soc. Am. Bull. 117 (9/10), 1242–1255.
Zdanowicz, C., Zielinski, G., Germani, M., 1999. Mount Mazama eruption: calendrical age verified and atmospheric impact assessed. Geology 27 (7), 621–624.